ADVANCED FUNCTIONAL MATERIALS
www.afm-journal.de

Metamaterial Adhesives-Integrated Triboelectric Nanogenerators with Enhanced and Programmable Charge Generation and Adhesion

Hee Jin Lee, Dong Kwan Kang, Junghwa Kang, Changwook Lee, Michael D. Bartlett, Junyeob Yeo,* and Hoon Eui Jeong**

Triboelectric nanogenerators (TENGs) harvest electrical energy from interfacial separation, yet achieving programmable and enhanced output through controlled separation mechanisms remains challenging. Here, a metamaterial adhesive-integrated TENG (MetaAdh-TENG) is presented that employs nonlinear cut architectures within an adhesive film embedded with silver nanowire (AgNW) electrodes. This structure enables spatially programmable and enhanced triboelectric charge generation and adhesion. Compared to planar counterparts, the MetaAdh-TENG exhibits a 12.8 fold increase in peak voltage (7.3 V) and a 34.8 fold enhancement in peel adhesion (202.3 N m^{-1}) by accelerating local crack velocity through crack trapping and reverse crack propagation. By tailoring the cut geometry, the charge output, adhesion strength, and their directionality can be independently and locally controlled, enabling tunable performance across a single device. These features support multifunctional applications, such as battery-free smart adhesives for fall detection and door-opening alarms, as well as roll-type systems for continuous charge generation.

1. Introduction

Interfacial contacts between distinct materials are central to a wide range of physical, chemical, and electrical phenomena, including adhesion,[1] friction,[2] and triboelectricity.[3] These interfacial interactions are directly associated with numerous practical applications. For instance, TENGs have emerged as a promising technology that harvests ambient mechanical energy from diverse sources.[4] By coupling triboelectrification with electrostatic induction, TENGs efficiently convert mechanical energy into usable electrical energy. To maximize versatility, TENG devices have been developed in various operational modes, such as vertical contact-separation,[5] lateral sliding,[6] and freestanding modes.[7] Fundamentally, all these operational modes fundamentally rely on the interfacial contact behavior between adjacent surfaces.

Adhesive technologies also depend on interfacial phenomena and are widely employed in applications ranging from household repairs to precision manufacturing. Recent advances in smart adhesives have introduced features such as tunable adhesion strength, switchable and directional adhesion, high reusability, and minimal surface damage.[8] These innovations have expanded their utility into emerging fields such as healthcare devices,[8a,9] soft robotics,[10] and pick-and-place manufacturing.[11] Particularly, programmable adhesives utilize strategies such as engineered cut patterns, mechanical metamaterials, or phase-change materials to enable spatially localized and tunable adhesion behaviors.[8b,c,f,12] Given their shared reliance on interfacial contact behavior, TENG technology and advanced adhesive systems offer strong potential for synergistic integration, enabling enhanced energy harvesting and multifunctional adhesion capabilities.

Despite this potential, integrating TENGs with adhesive technologies remains less explored. Adhesives generate charges during peeling processes at the contact interface. However, peeling-based TENG approaches face limitations, such as the need for high peel rates, discontinuous charge generation after peel-off, and relatively low charge output due to steady changes in the contact area during peeling.[13] Nevertheless, adhesive peeling represents a latent and underutilized source of mechanical energy

H. J. Lee, D. K. Kang, J. Kang, H. E. Jeong
Department of Mechanical Engineering
Ulsan National Institute of Science and Technology (UNIST)
Ulsan 44919, Republic of Korea
E-mail: hoonejeong@unist.ac.kr
C. Lee, J. Yeo
Department of Physics
Novel Applied Nano Optics Lab
Kyungpook National University
Daegu 41566, Republic of Korea
E-mail: junyeob@knu.ac.kr
M. D. Bartlett
Department of Mechanical Engineering
Soft Materials and Structures Lab
Virginia Tech
Blacksburg, VA 24061, USA
E-mail: mbartlett@vt.edu

The ORCID identification number(s) for the author(s) of this article can be found under https://doi.org/10.1002/adfm.202506293

DOI: 10.1002/adfm.202506293

that can be converted into electrical energy,[14] given the extensive use of adhesives in daily life and industrial applications. Furthermore, the development of peel-mode TENGs that support programmable charge generation and adhesion opens up new opportunities in diverse application domains.

Herein, we present a metamaterial adhesive-integrated TENG (MetaAdh-TENG) that locally controls interfacial crack propagation velocities to greatly enhance electrical energy generation. The MetaAdh-TENG device integrates nonlinear cut architectures with flexible AgNW electrodes into an adhesive film. This results in a 12.8x increase in peak voltage and a 34.8x enhancement in adhesion compared to planar TENG devices. These improvements arise from decoupling global interfacial separation rates from local separation rates through crack trapping and subsequent reverse crack propagation through the metamaterial adhesive cuts. This mechanism accelerates local crack velocities and boosts charge transfer at the contact interface. Importantly, our approach enables programmable control over multiple interfacial properties–including charge strength and location, adhesion strength and site, and directional behavior–by tailoring the geometry of the embedded cuts. Leveraging this programmability, we demonstrate the MetaAdh-TENG as a self-powered adhesive for detachment sensing, prevention, and continuous energy harvesting.

2. Results and Discussion

2.1. Structure and Working Mechanisms of MetaAdh-TENG

Figure 1a illustrates the conceptual design and working principle of the MetaAdh-TENG, which comprises multiple functional layers: a polyethylene terephthalate (PET) backing layer, a conductive electrode, and an adhesive layer interfacing with a dielectric substrate. The adhesive layer is made of polydimethylsiloxane (PDMS), and the electrode is formed by spray-coating AgNWs between the backing and adhesive layers (Figure S1, Supporting Information). AgNWs were selected due to their high electrical conductivity and excellent mechanical compliance. The flexible PET backing (modulus ≈2–4 GPa)[1a] constrains the elongation of the soft PDMS layer (≈1 MPa), thereby localizing interfacial strain and minimizing energy dissipation during detachment, which in turn improves triboelectric charge transfer. In addition to mechanical support, both PDMS and PET exhibit favorable triboelectric polarity[15] and moderate dielectric constants (≈2.8 and 3.0, respectively), enabling efficient charge separation and stable electrical insulation. Their high dielectric breakdown strength (100–500 kV mm^{-1}) ensures robustness under high electric fields.[16]

The MetaAdh-TENG incorporates nonlinear open-rectangular cuts into the adhesive layer, which are strategically designed to regulate interfacial crack propagation and enhance both adhesion and charge generation (Figure 1a). We refer to this structure as "MetaAdh-TENG" because the nonlinear cut architecture deliberately decouples global mechanical loading into localized adhesive and electrical responses, inspired by mechanical metamaterials capable of independently managing local and global deformation behaviors.[8c,17] This structural design also enables "spatial programmability" of triboelectric and adhesive responses across a single device. Specifically, by tailoring the geometry, dimensions, and orientation of the cuts during design and fabrication, both charge output and adhesion strength can be independently tuned at specific locations and directions. While the programmed characteristics remain static after fabrication, they enable diverse and spatially defined functionalities within a single film.

Upon initial contact with a substrate, the PDMS adhesive forms a conformal interface, leading to triboelectric charge accumulation on the surface and charge induction in the embedded electrodes via contact electrification and electrostatic induction. During peeling in the direction of maximum force, cracks propagate forward at a constant velocity until they reach the interconnect tips at the base of each cut (Figure 1b-i).[8c,f] In this regime, only weak adhesion and minimal charge generation occur, because of the limited rate of contact area change. When the cracks reach the interconnect tips, propagation is arrested, and further loading induces reverse crack propagation through the bonded sections (Figure 1b-ii). This inversion significantly increases adhesion by transforming a high global peel angle (θ) into a lower local peel angle (θ_α), thereby enhancing resistance to delamination through mechanical interlocking.[8c,f] As peeling proceeds, the patterned sections undergo abrupt delamination, resulting in a rapid change in the contact area and a corresponding spike in charge transfer between the top and bottom electrodes. This yields a sharp peak in triboelectric signal output (Figure 1b-iii). Once complete delamination occurs, the potential difference equilibrates, and electron flow–and thus signal generation–ceases (Figures S2 and S3, Supporting Information).

2.2. Electrical and Adhesion Performance of MetaAdh-TENG

To evaluate the electrical and adhesion performance of the MetaAdh-TENG, we employed a peel test setup (Figure S4, Supporting Information) with a device incorporating two rectangular cuts per row ($N_p = 2$, Figure S5, Supporting Information). The width (w_p), length (l_p), and interconnect width (w_{int}) were 10, 10, and 3.5 mm, respectively, across a 35 mm-wide (w) film (Figure S6, Supporting Information). A planar TENG without cuts served as control. For optimal performance, we used PDMS adhesive with a 15:1 base-to-curing-agent ratio and PET as the target substrate. These parameters yielded the highest voltage output and strongest adhesion among the tested configurations (see Figure S7, Supporting Information for details).

Figure 2a illustrates the dynamic peeling mechanism of the MetaAdh-TENG by simultaneously analyzing crack velocity (v_{crack}), triboelectric voltage, and peel force (F_c), supported by synchronized side- and bottom-view imaging (Figure 2a-i, ii). In Step 1, crack propagation in the unpatterned region proceeds at a constant velocity and peel force, with negligible voltage generation due to minimal contact area change ($t = 1.9$ s). In Step 2, as the crack approaches the patterned interconnect, it slightly accelerates but still produces minimal voltage (t = 2.3 s) due to gradual deformation and weak triboelectric polarization. In Step 3, the crack arrests at the tip of the interconnect, reducing peel velocity to nearly zero and halting charge generation ($t = 2.6$ s). In Step 4, continued mechanical loading triggers reverse crack propagation, which dynamically converts the global peel angle (θ) into a reduced local peel angle ($\theta_\alpha < 13°$). This nonlinear geometry

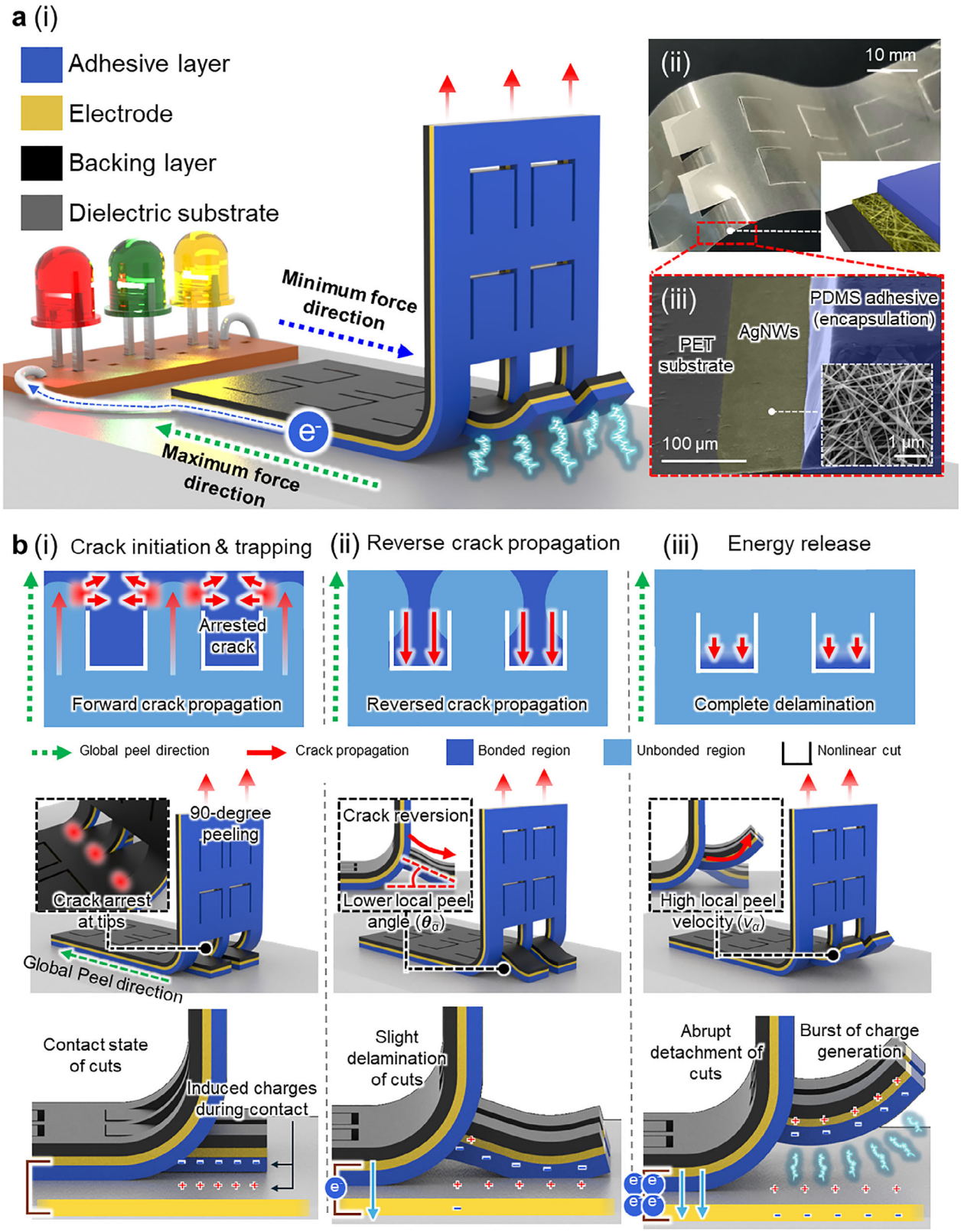

Figure 1. Structure and working mechanisms of the MetaAdh-TENG. a) (i) Conceptual illustration, (ii) photograph, and (iii) SEM image of the MetaAdh-TENG. b) Schematic of crack control and charge generation mechanisms during peeling in the maximum force direction.

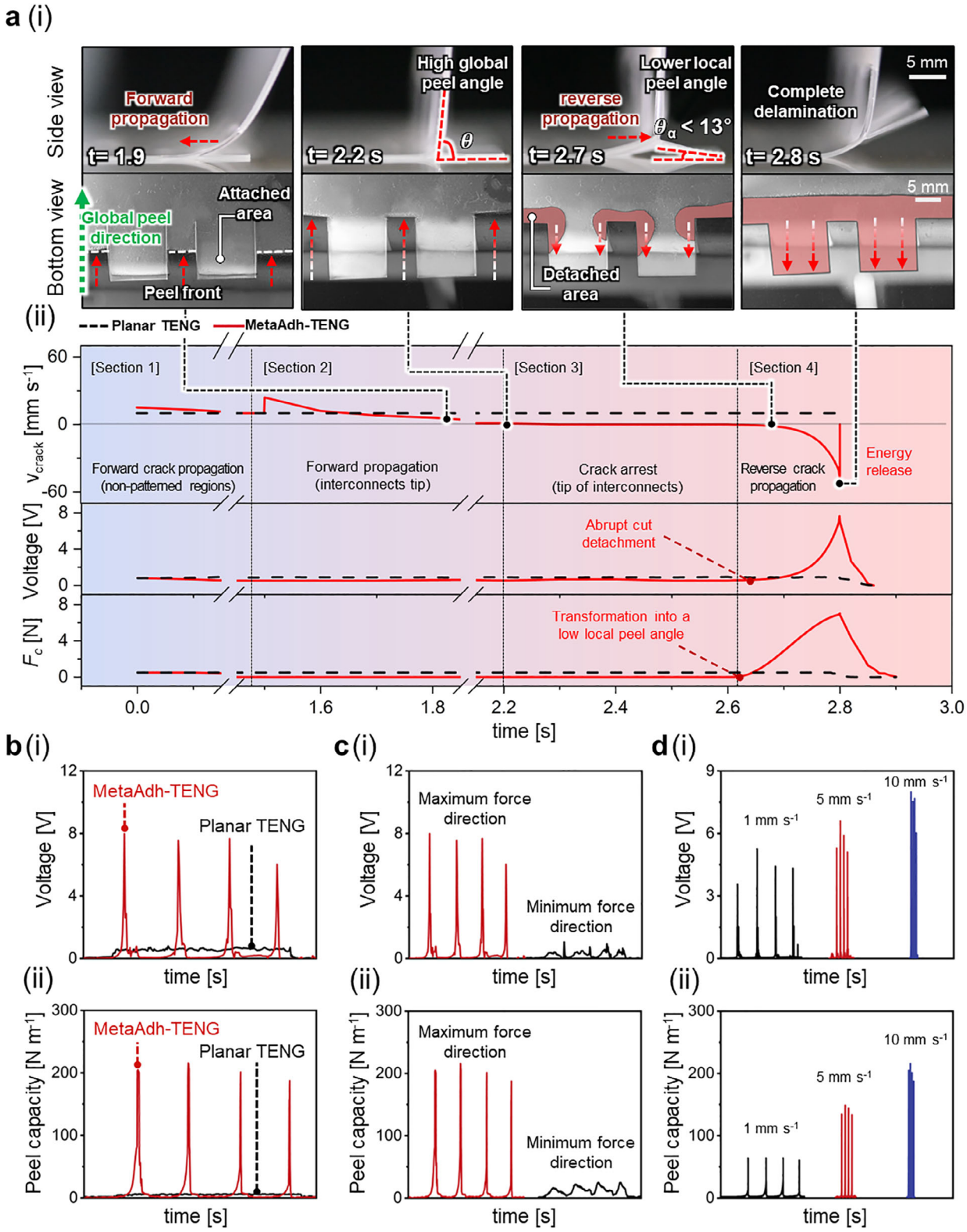

Figure 2. Electrical and adhesion performance of the MetaAdh-TENG. a) (i) Sequential side- and bottom-view images of the peeling process in the maximum force direction, and (ii) corresponding-time time-dependent crack velocity, peel force, and voltage output. b) Comparison of (i) voltage output and (ii) peel adhesion between the MetaAdh-TENG and a planar TENG at a peel rate of 10 mm s^{-1}. c) (i) Voltage output and (ii) peel adhesion of the MetaAdh-TENG under peeling in the maximum and minimum force directions at 10 mm s^{-1}. d) (i) Voltage output and (ii) peel adhesion of the MetaAdh-TENG at different peel rates in the maximum force direction.

causes abrupt delamination of the cut segments, during which the local crack velocity (v_a) exceeds 500 mm s^{-1} (Figure S8 and Movie S1, Supporting Information), while the global peel rate remains at 10 mm s^{-1}. This rapid local detachment significantly alters the contact area and electric field distribution, leading to a sharp voltage spike due to intense, localized charge separation ($t = 2.7$ s).

These peeling behaviors follow classical peel mechanics, where the peel force F_c is given by:[18]

$$F_c = \frac{G_c \cdot \omega}{1 - \cos\theta} \quad (1)$$

where G_c is the interfacial fracture energy, ω is the width of the peeling film, and θ is the peel angle. This relationship implies that a reduction in the local peel angle, as observed in the MetaAdh-TENG, results in higher resistance to delamination and thereby a greater effective peel force. In contrast, the planar TENG exhibits uninterrupted crack propagation, which sustains a relatively high peel angle (θ) (Figure S9, Supporting Information), resulting in weak adhesion and a low voltage output (≈0.57 V).

The enhanced charge transfer in the MetaAdh-TENG can be understood by considering the short-circuit charge generation in a peeling-based TENG:[19]

$$Q_{SC}(t) \approx \frac{A(t) \cdot \sigma \cdot \bar{x}(t)}{d_0 + \bar{x}(t)} \quad (2)$$

where $A(t)$ is the contact area, σ is the surface charge density, $\bar{x}(t)$ is the distance between electrodes and d_0 is the effective dielectric thickness. In the MetaAdh-TENG, crack arrest followed by reverse propagation leads to the abrupt engagement of a larger contact area $A(t)$ and a rapid shift in $\bar{x}(t)$ within a short time window–particularly during dynamic crack reversal. These transient geometric and mechanical changes collectively result in more efficient charge transfer compared to the planar TENG, which lacks such discontinuities.

Figure 2b and Table S1 (Supporting Information) compare the performance under repeated peeling at 10 mm s^{-1} in the maximum force direction: the MetaAdh-TENG generates burst-like voltages averaging 7.3 V–a 12.8 fold increase over the planar TENG–induced by sudden changes in contact area, separation distance, and crack direction. The corresponding peel adhesion energy also increases substantially, reaching over 202.3 N m^{-1} compared to 7 N m^{-1} for the planar TENG–a 34.8 fold enhancement. These results demonstrate the critical role of nonlinear geometry in enabling synchronized improvements in mechanical adhesion and charge output.

Metamaterial adhesives with nonlinear cuts offer programmable adhesion directionality,[8c,f] as reflected in the MetaAdh-TENG's triboelectric and adhesion performance. In the maximum force direction, the device generated an average voltage of 7.3 V, whereas only 0.71 V was obtained in the opposite direction, yielding a voltage directionality (V_{max}/V_{min}) of 10.3 (Figure 2c-i). Similarly, the peel adhesion energy was highly directional, showing a ratio of 9.8× (Figure 2c-ii). This performance also varied with peel rate (Figure 2d): as the rate increased from 1 mm s^{-1} to 5 and 10 mm s^{-1}, output voltages rose from 4.4 to 5.7, and 7.3 V, respectively, driven by more abrupt electric field changes at higher speeds (Figure S8 and Table S2, Supporting Information).[20] Adhesion energy followed the same trend, increasing from 63 to 139.8 and 202.3 N m^{-1}.[1a,21]

2.3. Design Effects

The MetaAdh-TENG enables easy programmability of its triboelectric and adhesive properties through simple modifications to the geometry of its cuts. **Figure 3**a shows the electrical signals generated by the MetaAdh-TENG with varying cut lengths (l_p) at two different peel rates: 10 mm s^{-1} (Figure 3a-i) and 100 mm s^{-1} (Figure 3a-ii). The spacing (s) between the rows of cuts was equal to the l_p of each sample. The output peak voltage increased monotonically from 3.3 to 17.2 V as l_p increased from 5 to 30 mm at a peel rate of 10 mm s^{-1} (Figure 3a-i). This increase arises from enhanced contact area variation during abrupt detachment of the cut regions, which scale with l_p. A similar trend was observed at a peel rate of 100 mm s^{-1}, with higher voltages generated compared to those at 10 mm s^{-1} (Figure 2g). Increasing the pattern width (w_p) also resulted in higher output voltage when the number of pattern cuts (N_p) remained constant ($N_p = 2$) (Figure 2b). This is because a larger w_p leads to greater contact area change per cut under a fixed N_p, thereby enhancing triboelectric charge transfer and boosting output voltage.

Next, we investigated the optimal N_p for the MetaAdh-TENG while keeping the total film width constant ($w = 35$ mm). As N_p increased from 1 to 4, the width of individual pattern cuts (w_p) decreased proportionally from 20 to 5 mm. Figure 3c-i-iii show that variations in N_p did not significantly affect output voltage when the total device width was fixed. All configurations exhibited similar output voltages due to essentially identical changes in contact area. This suggests that total contact area change, rather than the number or width of individual cuts, is the key factor influencing electrical output when the overall dimensions are fixed.

In contrast, peel capacity was affected by both N_p and w_p. Previous studies have shown that maximum crack trapping occurs when half the cut width exceeds a critical length (l_{ch}) ($0.5w_p > l_{ch}$).[8c,f] Under this condition, cracks originating at each tip of interconnects do not overlap, maximizing peel strength. The critical length, l_{ch}, is determined by the equation:[8c,f]

$$l_{ch} = \sqrt{\frac{2D}{G_c}\frac{w_{int}}{w}\left(N_p^* + 1\right)} \quad (3)$$

where D represents the flexural rigidity of the adhesive film, G_c is the critical energy release rate or adhesion energy, and N_p^* is the optimal number of cuts. Since G_c varies with peel rates, the calculated l_{ch} values were found to be 4.91 and 2.82 for the peel rates of 10 mm s^{-1} and 100 mm s^{-1}, respectively (Figure S10, Supporting Information). Accordingly, peel capacity was maximized at 202.3 N m^{-1} with $N_p = 2$ ($w_p = 10$ mm) at 10 mm s^{-1} (Figure 3c-ii) and at 580 N m^{-1} with $N_p = 3$ ($w_p = 6.7$ mm) at 100 mm s^{-1} (Figure 3c-iv).

Figure 3d depicts a MetaAdh-TENG with varying rectangular cut designs across its surface, enabling programmable output voltage and peel capacity. The cuts at locations 1, 2, and 3 measured 10 mm (w_p) x 10 mm (l_p), 10 mm x 5 mm, and 5 mm

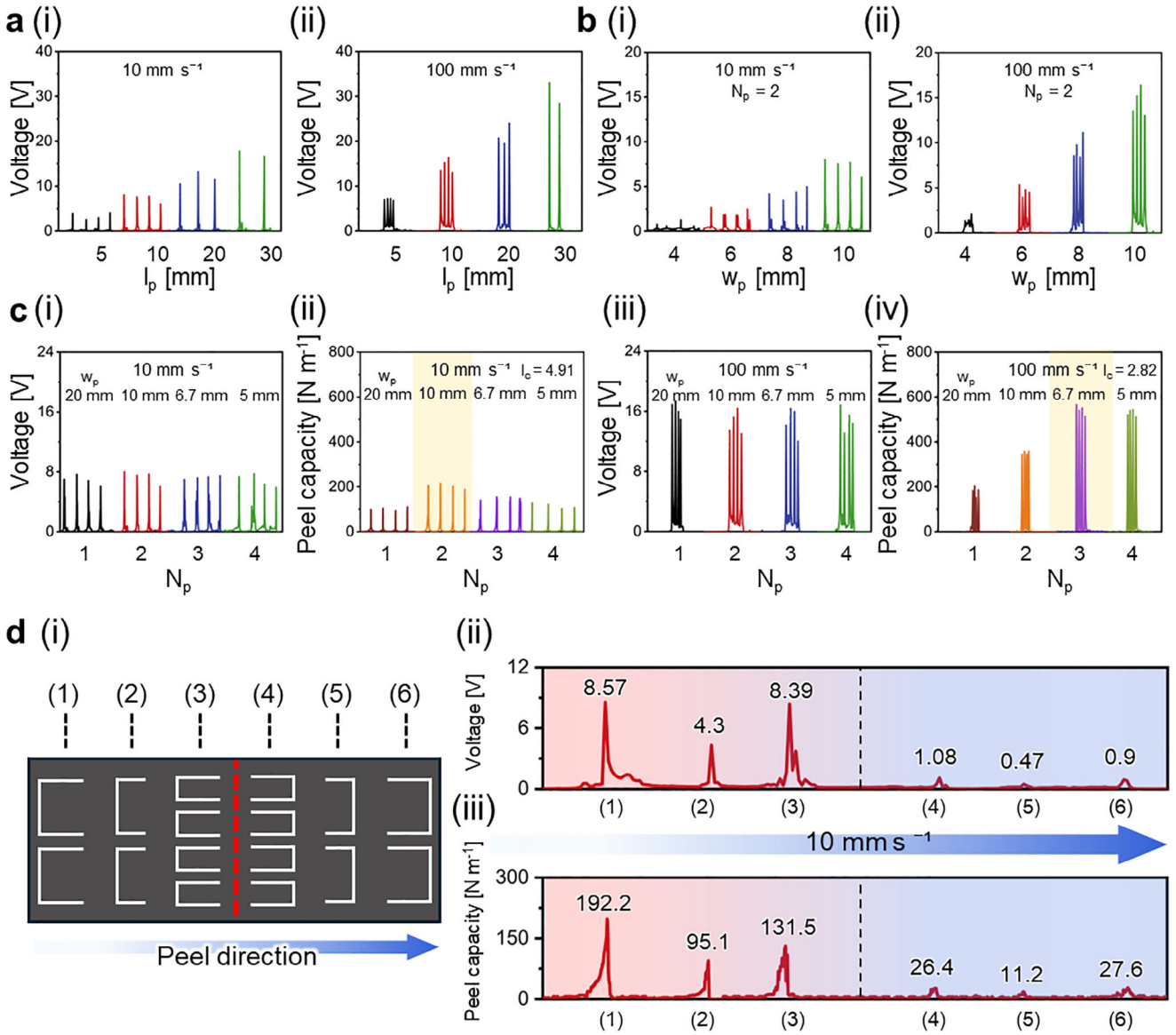

Figure 3. Design effects on the electrical and adhesion performance of the MetaAdh-TENG. a) Voltage output with varying cut lengths (l_p) at peel rates of (i) 10 mm s^{-1} and (ii) 100 mm s^{-1}. b) Voltage output with varying cut widths (w_p) at (i) 10 mm s^{-1} and (ii) 100 mm s^{-1} ($N_p = 2$). c) (i, ii) Voltage output and peel adhesion with varying numbers of cuts (N_p) at 10 mm s^{-1}; (iii, iv) same measurements at 100 mm s^{-1}. d) (i) MetaAdh-TENG with heterogeneous cut designs across its surface; (ii) Voltage output and (iii) peel adhesion at different locations under left-to-right peeling at 10 mm s^{-1}.

x 10 mm, respectively. Cuts at locations 4, 5, and 6 had the same dimensions as those at 1, 2, and 3, but in reverse orientations. When the device was peeled from left to right, the peak voltage and peel adhesion at location 1 were 8.6 V and 192.2 N m^{-1}, while they decreased to 4.3 V and 95.1 N m^{-1} at location 2. The voltage at location 3 was 8.4 V, similar to that at location 1 due to comparable contact areas. However, the peel adhesion at location 3 was 131.5 N m^{-1} (68.4% of location 1). These results demonstrate that output voltage and adhesion can be independently controlled by adjusting the cut design. The voltage and peel adhesion at locations 4, 5, and 6 were minimized due to uninterrupted crack propagation without arrest or reversion.

2.4. Electrical Properties

We investigated additional electrical properties of the MetaAdh-TENG using two different nonlinear cut designs (**Figure 4a**). Figure 4b shows the transferred charge during the peeling of MetaAdh-TENG (design 1) at a rate of 10 mm s^{-1}. Evaluating transferred charge in a TENG is crucial, as it underpins the fundamental mechanism of electricity generation. When peeled in the maximum force direction, minimal charge transfer occurred as the crack propagated forward. However, reverse crack propagation induced by the cuts accelerated crack velocity, abruptly increasing charge transfer. Consequently, after complete

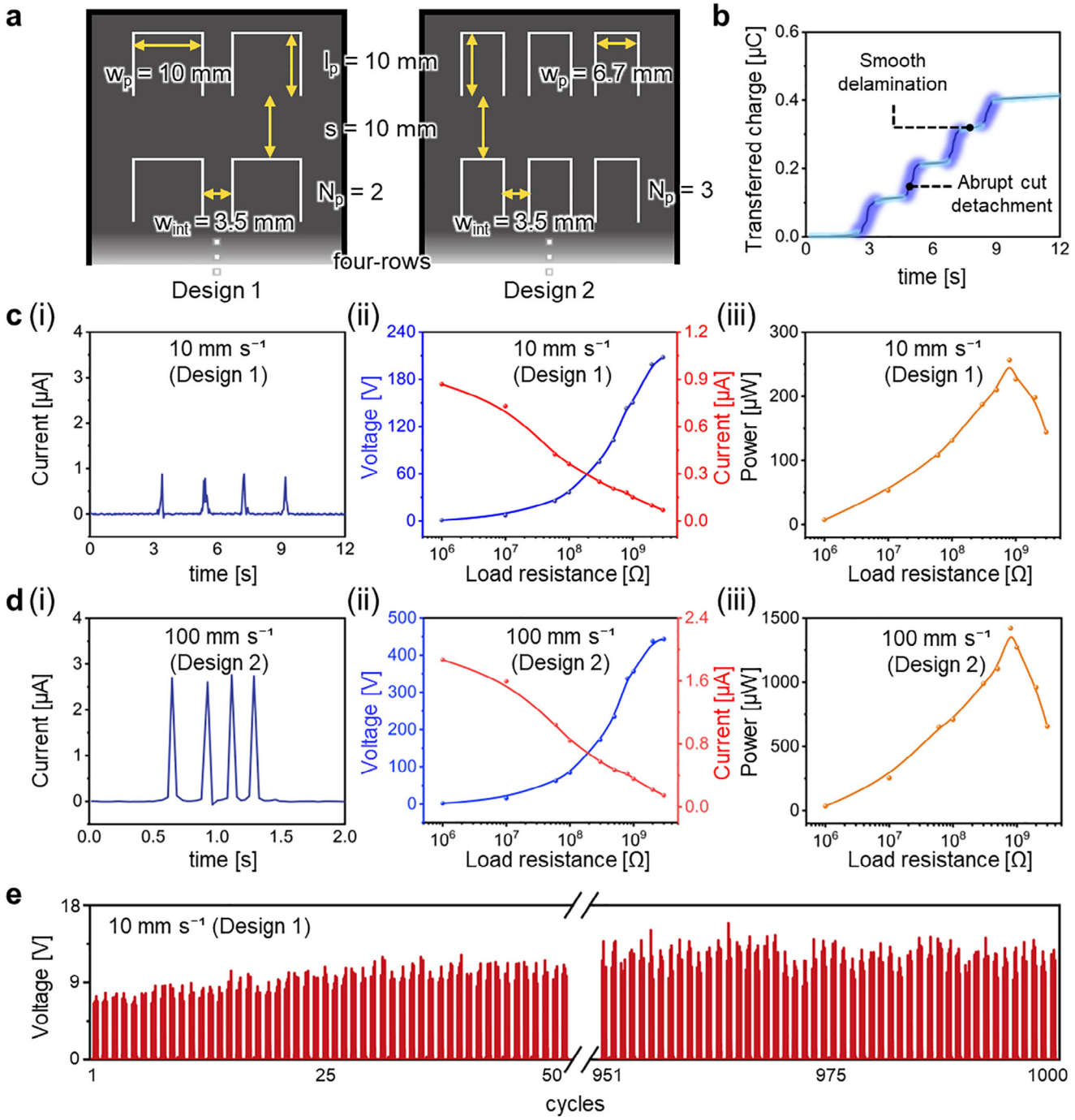

Figure 4. Electrical properties of MetaAdh-TENG. a) Schematic of two cut designs used for electrical performance tests. b) Transferred charge of design 1 during maximum-force directional peeling at 10 mm s^{-1}. c) Electrical performance of design 1: (i) current output during peeling at 10 mm s^{-1}, (ii) voltage and current as functions of load resistance, and (iii) corresponding power output. d) Electrical performance of design 2: (i) current output during peeling at 100 mm s^{-1}, (ii) voltage and current as functions of load resistance, and (iii) corresponding power output. e) Voltage stability of design 1 over 1,000 attachment–detachment cycles (peel rate = 10 mm s^{-1}).

delamination of four rows of cuts, the total transferred charge reached 0.41 μC.

Figure 4c-i presents the current output of design 1 at a peel rate of 10 mm s^{-1}. This rate was chosen as it maximizes the device's adhesion properties (Figure 3c). The device exhibited sharp current peaks, averaging 0.83 μA, each time a patterned cut delaminated. According to the equation, $I = dQ/dt$, these current peaks occur when the charge is transferred rapidly. In contrast, the planar TENG exhibited significantly lower current peaks (0.058 μA) under identical conditions (Figure S11, Supporting Information).

We further evaluated the voltage and current of the MetaAdh-TENG under varying load resistances (Figure 4c-ii). As expected from Ohm's law, the voltage increased linearly from near 0 to 201 V, while the current decreased to nearly 0 as the load resistance increased from 100 kΩ to 3 GΩ. The power output, calculated using $P = I^2R$ (Figure 4c-iii), peaked at 256.69 μW at 800 MΩ.

The MetaAdh-TENG with design 2 exhibited similar trends in current, voltage, and power compared to design 1, but with overall higher output values: an average current of 2.73 μA (Figure 4d-i), a maximum voltage of 436 V (Figure 4d-ii), and a peak power of 1423 μW (Figure 4d-iii). For design 2, the peel rate was set at 100 mm s^{-1} to match its maximized peel adhesion characteristics (Figure 3c). To assess long-term durability, we performed repeated mechanical cycling and time-lapse testing. The device maintained stable voltage output over 1000 attachment–detachment cycles at a peel rate of 10 mm s^{-1}, showing a slight voltage increase due to gradual surface charge accumulation. (Figure 4e).[22] It also retained consistent adhesion performance over 1000 repeated cycles (Figure S12, Supporting Information). We also measured the voltage output on days 1, 5, 10, 15, and 30, during which the device consistently delivered peak performance without noticeable degradation (Figure S13, Supporting Information). These results confirm that the MetaAdh-TENG maintains mechanical and electrical robustness under both repeated use and extended operation.

We further evaluated environmental stability by varying relative humidity (30–80%) and temperature (25–100 °C) at a constant peel rate of 10 mm s^{-1}. The peak output voltage decreased with increasing humidity and temperature, consistent with prior reports (Figure S14, Supporting Information).[23] In particular, high humidity likely suppresses surface charge retention and promotes charge dissipation.[23] Additional tests confirmed that the device maintained recoverable performance after UV exposure, surface contamination, and direct moisture contact, demonstrating its robustness under realistic environmental conditions (Figure S15, Supporting Information).

2.5. Application

The MetaAdh-TENG offers programmable electrical and adhesion capabilities, making it suitable for applications requiring both charge generation and reliable adhesion. This enables untethered, battery-free operation of self-powered devices. As a demonstration, we developed a MetaAdh-TENG that secures an object to a wall and detects unintended detachment (**Figure 5**a). The device features a 3 × 5 array of rectangular cuts (Figure 5a-i), with narrower outer rows designed to lower adhesion compared to the center. This configuration allows the side cuts to delaminate earlier, generating an initial electrical signal while the central cuts continue to support the object, allowing time to prevent complete detachment. The signal is transmitted wirelessly to a smartphone via Bluetooth (Figure 5a-ii).

Figure 5a-iii shows the MetaAdh-TENG securing a 300 g frame, which partially detached after three days. Upon detachment, it sent a smartphone alert without needing an external power source. Similarly, a 700 g clock was secured using the device. When it fell, the MetaAdh-TENG detected the event with a higher signal due to its weight. The central cuts helped prevent complete detachment, demonstrating self-sustained adhesion.

The MetaAdh-TENG also works as a door sensor to protect valuable items without external power. For this, a 2 × 6 rectangular cut pattern was used (Figure 5b-i), split between the door and wall. When forced open, it resisted detachment and generated a >9 V peak, activating a buzzer (Figure 5b-ii, iii; Movie S2, Supporting Information).

The MetaAdh-TENG can be integrated into a roller-based system for continuous charge generation. **Figure 6**a-i illustrates a planar substrate with patterned cuts, over which a roller with a PET encapsulation layer and core electrode travels. When rolling in the maximum force direction, the device generates an average peak voltage of 4.3 V, compared to 1 V in the minimum direction (Figure 6a-ii). Continuous rolling enables sustained charge generation. Increasing the rolling frequency (50–300 Hz) further boosts voltage output due to abrupt segment detachment and shortened contact–separation intervals, which reduce charge recombination and enhance charge accumulation (Figure S16, Supporting Information).

Figure 6b-i shows a conveyor system where an auxiliary MetaAdh-TENG detects belt rotation (Figure S17, Supporting Information). In the intended clockwise motion, it rotates counterclockwise without detachment, generating <1 V (Figure 6b-ii, iv, vi). Reverse rotation causes clockwise motion in the maximum force direction (Figure 6b-iii), leading to abrupt detachment and 4.2 V peaks, which trigger an alarm and stop the system (Figure 6b-v, vi; Movie S3, Supporting Information). Besides direction sensing, the system also charged capacitors and powered a 33-LED array, confirming its energy harvesting capability (Figure S16, Supporting Information). While not evaluated in this study, the materials used in the MetaAdh-TENG–such as PDMS and AgNWs–have been widely reported to exhibit biocompatibility and low cytotoxicity,[8f,24] supporting their potential for future wearable applications.

3. Conclusion

In summary, we introduced a TENG integrated with metamaterial adhesives that enables spatially programmable charge generation and adhesion. This system provides a versatile platform for concurrently tuning interfacial adhesion and electrical output–an area that remains largely unexplored. The MetaAdh-TENG, incorporating rationally designed nonlinear cuts, exhibited substantially enhanced peak voltage and adhesion compared to a planar TENG. These improvements stemmed from controlled crack trapping and reverse propagation mechanisms induced by the patterned cuts, which facilitated efficient charge transfer at the interface. As a result, the device achieved a peak voltage of 7.3 V and adhesion energy of 202.3 N m^{-1} at a peel rate of 10 mm·s^{-1}–12.8× and 34.8× greater, respectively, than the control. At 100 mm s^{-1}, it further reached 14.5 V and 350.9 N m^{-1}. Notably, the MetaAdh-TENG demonstrated strong directional dependence (≈10) in both electrical and adhesive performance.

Importantly, the electrical and adhesion properties of the MetaAdh-TENG can be fully customized by varying the size and orientation of the nonlinear pattern cuts, enabling precise, spatially programmable, multidirectional control. Further performance enhancements are expected through the integration of

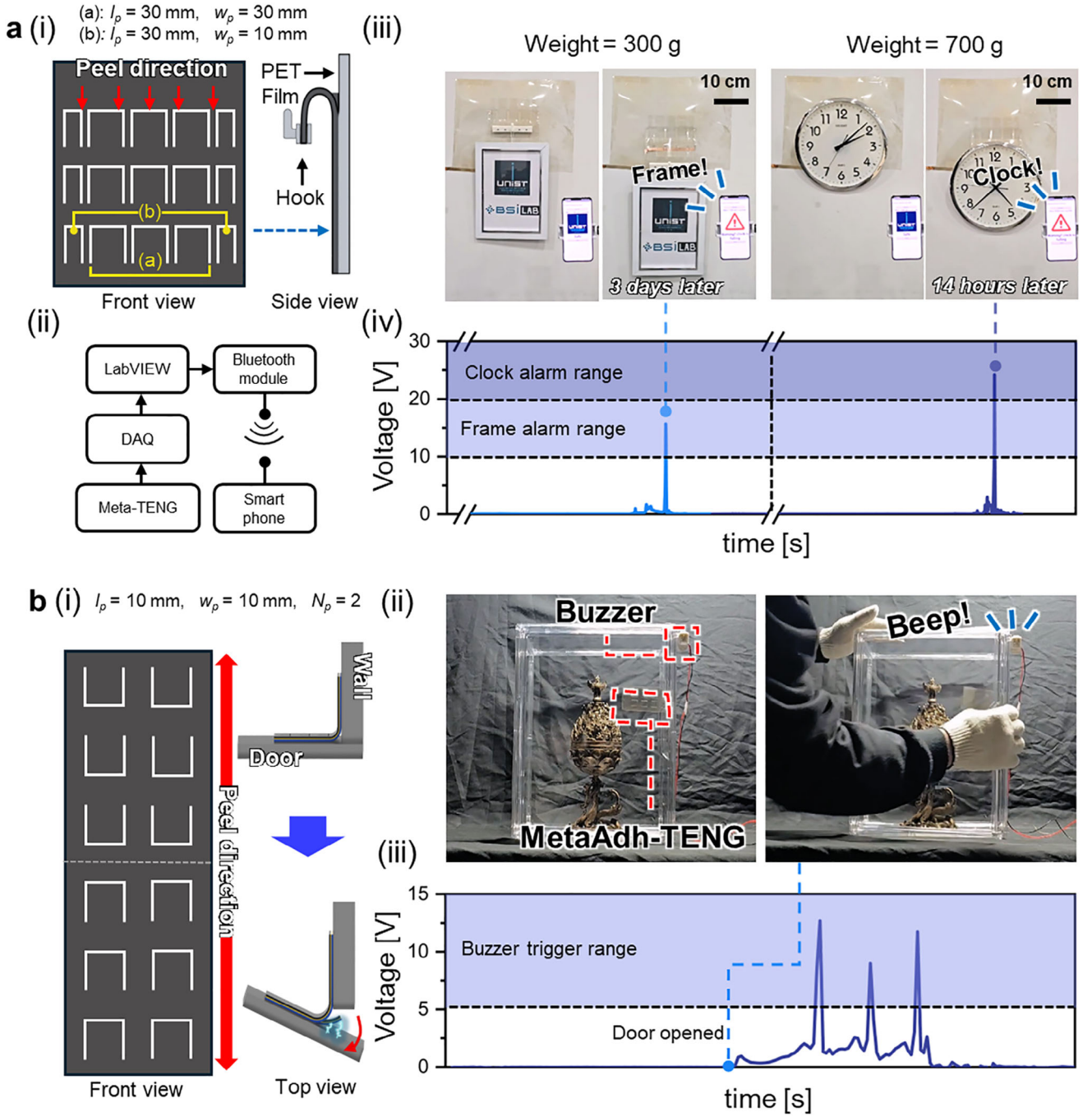

Figure 5. Application of the MetaAdh-TENG. a) Wall-mounted object monitoring: (i) device schematic, (ii) system configuration, (iii) photos of 300 g frame and 700 g clock with fall detection, (iv) voltage output during fall. b) Door monitoring: (i) device schematic, (ii) photos of sensing during door opening, (iii) corresponding voltage signal.

bioinspired adhesive architectures,[8a,25] megastructures,[26] surface modifications,[27] alternative cut geometries,[8b,f,28] or advanced nanomaterials.[29] With its programmable adhesion and charge generation, the MetaAdh-TENG supports practical applications that demand both functions, such as smart warning adhesives for detecting forced changes (e.g., falling objects, door openings) and roll-type systems for continuous energy harvesting.

While the current MetaAdh-TENG exhibits static, predesigned programmability, it does not yet support active, externally controlled modulation of adhesion and electrical output. Integrating stimuli-responsive materials, such as thermally or electrically actuated phase-change polymers, could enable real-time modulation of adhesion and triboelectric outputs.[8a] This dynamic programmability, triggered by external stimuli such as voltage, strain, temperature, or humidity, represents a promising future

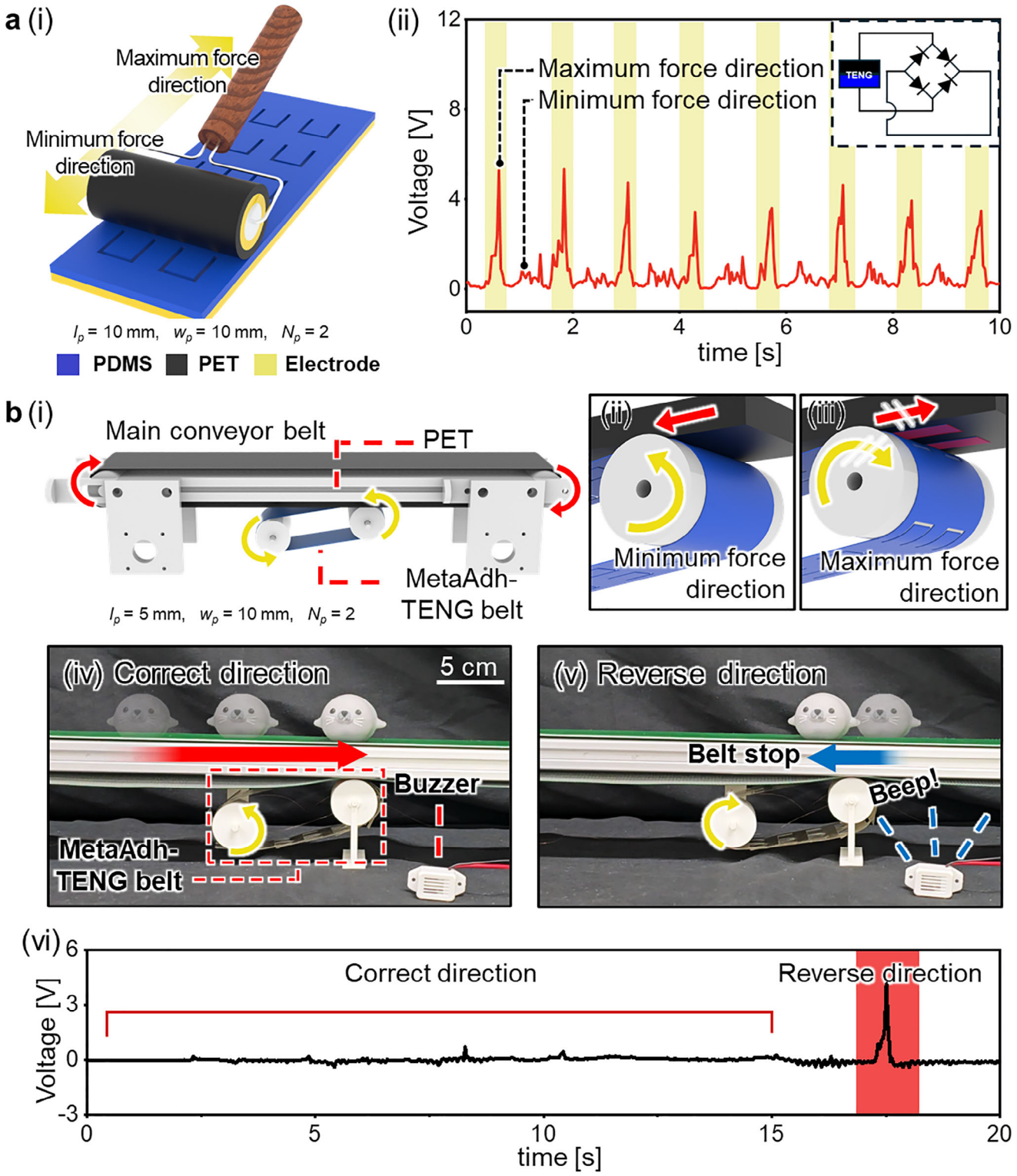

Figure 6. MetaAdh-TENG integration in rolling-based systems. a) (i) Roller over a substrate with patterned cuts for continuous charge generation; (ii) voltage output during bidirectional rolling. b) Conveyor system with auxiliary MetaAdh-TENG for rotation sensing: (i) system schematic; (ii) counterrotation during normal operation; (iii) clockwise rotation during reverse motion; (iv) normal state; (v) alarm-triggered shutdown; (vi) voltage signal.

direction. We anticipate that the MetaAdh-TENG will be compatible with commercial materials and scalable manufacturing methods, and thus will drive advancements in smart adhesives, TENGs, wearable devices, intelligent manufacturing, and various self-powered systems.

4. Experimental Section

Fabrication of MetaAdh-TENG: First, one side of a 100 µm-thick PET film (SKC, Republic of Korea) was spray-coated with an AgNW solution containing 0.5 wt% AgNWs (A40, 40 nm × 35 µm, 10 mg mL^{-1} in DI water, Novarials, USA) to form an electrode. The AgNW electrode achieved a sheet resistance of <5 Ω cm^{-2}. Cu wires were attached to the AgNW electrode using Ag paste (P-100, ELCOAT, Republic of Korea) to establish electrical connections. Next, a PDMS solution was prepared by mixing the base prepolymer and curing agent at varying weight ratios, followed by degassing in a vacuum chamber for 30 min. The PDMS mixture was then uniformly applied over the AgNW-coated PET film to a thickness of 100 µm using the doctor blade method and cured at 80 °C for 1 h in a convection oven. Finally, nonlinear cuts were introduced into the PDMS–PET–AgNW multilayer using a computer-controlled cutting plotter (Silhouette CAMEO 4, Silhouette Inc., USA), which provides a cutting resolution of up to 0.1 mm. The cutting path was generated from a CAD file defining the dimensions and layout of the nonlinear patterns. Using proprietary control software, the plotter executed the cutting process with a 1 mm-deep fine-point blade under digitally controlled speed and force settings, enabling accurate and repeatable patterning of the multilayered structure. This step completed the fabrication of the MetaAdh-TENG device (Figure S1, Supporting Information).

Adhesion Tests: The peel adhesion characteristics of the MetaAdh-TENG were assessed against various substrates using a 90° peel test on a custom-built adhesion tester equipped with a 20 N load cell (LFT-25-2KG, Cellscale, Netherlands) and a linear motor (HM01-23 × 160, LinMot, USA) (Figure S4, Supporting Information). Tests were conducted at retraction rates of 1–100 mm s^{-1}. Substrates were mounted on a horizontally slidable stage using double-sided tape (3M, USA). The MetaAdh-TENG was then pressed against the substrate using a rubber roller. The free end of the sample was fixed to a vertically moving jig connected to the tester, and adhesive forces were recorded as the jig moved upward.

Electrical Tests: Electrical and charge generation characteristics were evaluated using the same peel test setup. During peeling, the AgNW electrodes embedded between the PDMS and PET layers and on the substrate were connected to measurement probes (Figure S4, Supporting Information). The voltage, short-circuit current, and transferred charge were recorded using a data acquisition system (DAQ970A, Keysight, USA) and an electrometer (Keithley 6514, Keithley, USA). The local delamination velocity of the patterned cuts was recorded at 500 fps using a high-speed camera (FASTCAM SA3, Phantom, USA).

Supporting Information

Supporting Information is available from the Wiley Online Library or from the author.

Acknowledgements

H.J.L., and D.K.K. contributed equally to this work. This work was supported by the National Research Foundation of Korea grant funded by the Korean government (MSIT) (NRF-2021R1A2C3006297/RS-2024-00432685/RS-2025-00562249).

Conflict of Interest

The authors declare no conflict of interest.

Data Availability Statement

The data that support the findings of this study are available from the corresponding author upon reasonable request.

Keywords

interfacial crack, kirigami, mechanical metamaterials, smart adhesive, TENG

Received: March 10, 2025
Revised: May 13, 2025
Published online:

[1] a) M. D. Bartlett, S. W. Case, A. J. Kinloch, D. A. Dillard, *Prog. Mater. Sci.* **2023**, *137*, 101086; b) Z. Gu, S. Li, F. Zhang, S. Wang, *Adv. Sci. (Weinh)* **2016**, *3*, 1500327.
[2] a) A. Jagota, C.-Y. Hui, *Mater. Sci. Engin.: R: Rep.* **2011**, *72*, 253; b) M. Nosonovsky, B. Bhushan, *Mater. Sci. Engin.: R: Rep.* **2007**, *58*, 162.
[3] a) Y. Fang, C. K. Ao, Y. Jiang, Y. Sun, L. Chen, S. Soh, *Nat. Commun.* **2024**, *15*, 1986; b) Z. L. Wang, A. C. Wang, *Mater. Today* **2019**, *30*, 34.
[4] F.-R. Fan, Z.-Q. Tian, Z. Lin Wang, *Nano Energy* **2012**, *1*, 328.
[5] a) M. Guo, Y. Xia, J. Liu, Y. Zhang, M. Li, X. Wang, *Adv. Funct. Mater.* **2025**, *35*, 2419209; b) C. Jin, C. Zhang, P. Yan, M. Jiang, R. Yin, K. Li, W. Zhao, Z. Bai, *Adv. Funct. Mater.* **2024**, *34*, 2402233; c) J. Li, Y. Liu, M. Wu, K. Yao, Z. Gao, Y. Gao, X. Huang, T. H. Wong, J. Zhou, D. Li, H. Li, J. Li, Y. Huang, R. Shi, J. Yu, X. Yu, *Fundam Res* **2023**, *3*, 111.
[6] a) G. Li, S. S. An, P. Wang, S. Y. Xiong, J. Wang, S. Y. Xu, H. Y. Wu, K. X. Li, W. Li, L. Tong, C. G. Hu, *Adv. Funct. Mater.* **2025**, *35*, 2413359; b) Y. F. Wang, X. D. Lin, G. Y. Gao, J. R. Yu, Y. C. Wei, J. Gong, J. Sun, Z. L. Wang, Q. J. Sun, *Adv. Funct. Mater.* **2024**, *34*, 2313210.
[7] a) S. H. Du, S. K. Fu, W. C. He, Q. Y. Li, K. X. Li, H. Y. Wu, J. Wang, C. C. Shan, Q. J. Mu, C. G. Hu, *Adv. Funct. Mater.* **2023**, *33*, 2306491; b) Z. J. Li, S. X. Zhang, H. Y. Guo, B. Wang, Y. Gong, S. Y. Zhong, Y. Peng, J. Y. Zheng, X. H. Xiao, *Nano Energy* **2023**, *113*, 108595.
[8] a) G. Choi, J. Kim, H. Kim, H. Bae, B. J. Kim, H. J. Lee, H. Jang, M. Seong, S. M. Tawfik, J. J. Kim, H. E. Jeong, *Adv. Mater.* **2025**, *37*, 2412271; b) D. Hwang, C. Lee, M. D. Bartlett, *Philos. Trans. A Math. Phys. Eng. Sci.* **2024**, *382*, 20240011; c) D. Hwang, C. Lee, X. Yang, J. M. Perez-Gonzalez, J. Finnegan, B. Lee, E. J. Markvicka, R. Long, M. D. Bartlett, *Nat. Mater.* **2023**, *22*, 1030; d) D. G. Hwang, K. Trent, M. D. Bartlett, *ACS Appl. Mater. Interfaces* **2018**, *10*, 6747; e) H. J. Park, M. Kim, J. Lee, M. K. Kwak, *Adv. Sci. (Weinh)* **2024**, *11*, 2309393; f) S. Park, D. K. Kang, D. Lee, G. Choi, J. Kim, C. Lee, M. Seong, M. D. Bartlett, H. E. Jeong, *Sci. Adv.* **2024**, *10*, adq3438.
[9] a) I. Hwang, H. N. Kim, M. Seong, S. H. Lee, M. Kang, H. Yi, W. G. Bae, M. K. Kwak, H. E. Jeong, *Adv. Healthcare Mater.* **2018**, *7*, 1800275; b) J. H. Shin, J. Y. Choi, K. June, H. Choi, T. I. Kim, *Adv. Mater.* **2024**, *36*, 2313157.
[10] a) Z. Chen, Y. Wang, H. Chen, J. Law, H. Pu, S. Xie, F. Duan, Y. Sun, N. Liu, J. Yu, *Nat. Commun.* **2024**, *15*, 644; b) S. Park, G. Choi, M. Kang, W. Kim, J. Kim, H. E. Jeong, *Microsyst. Nanoengineering.* **2023**, *9*, 153.
[11] a) H. Liu, H. Tian, D. Wang, T. Yuan, J. Zhang, G. Liu, X. Li, X. Chen, C. Wang, S. Cai, J. Shao, *Sci. Adv.* **2023**, *9*, adj3133; b) M. Seong, K. Sun, S. Kim, H. Kwon, S. W. Lee, S. C. Veerla, D. K. Kang, J. Kim, S. Kondaveeti, S. M. Tawfik, H. W. Park, H. E. Jeong, *Nat. Commun.* **2024**, *15*, 7929.
[12] Q. Li, W. X. Liu, C. H. Yang, P. Rao, P. Y. Lv, H. L. Duan, W. Hong, *J. Mech. Phys. Solids* **2022**, *169*, 105053.
[13] a) Y. I. Sobolev, W. Adamkiewicz, M. Siek, B. A. Grzybowski, *Nat. Phys.* **2022**, *18*, 1347; b) L. Q. Zhang, Y. L. Zhang, X. J. Li, Y. E. Feng, B. Yu, F. Zhou, D. A. Wang, *Nano Energy* **2022**, *95*, 107011.

[14] a) K. Shi, B. Chai, H. Zou, Z. Wen, M. He, J. Chen, P. Jiang, X. Huang, *Adv. Funct. Mater.* **2023**, *33*, 2307678; b) H. Stöcker, M. Rühl, A. Heinrich, E. Mehner, D. C. Meyer, *J. Electrostat.* **2013**, *71*, 905; c) H. Zhang, S. Feng, D. He, Y. Xu, M. Yang, J. Bai, *Nano Energy* **2018**, *48*, 256.

[15] a) T.-C. Hou, Y. Yang, H. Zhang, J. Chen, L.-J. Chen, Z. Lin Wang, *Nano Energy* **2013**, *2*, 856; b) G.-Z. Li, Y.-W. Cai, G.-G. Wang, N. Sun, F. Li, H.-L. Zhou, X.-N. Zhang, H.-X. Zhao, Y. Wang, J.-C. Han, Y. Yang, *Nano Energy* **2022**, *99*, 107423.

[16] D. Q. Tan, *J. Appl. Polym. Sci.* **2020**, *137*, 49379.

[17] a) C. W. Peterson, T. Li, W. Jiang, T. L. Hughes, G. Bahl, *Nature* **2021**, *589*, 376; b) A. Tanay, A. Regev, *Nature* **2017**, *541*, 331.

[18] K. Kendall, *J. Phys. D: Appl. Phys.* **1975**, *8*, 1449.

[19] a) S. Niu, S. Wang, L. Lin, Y. Liu, Y. S. Zhou, Y. Hu, Z. L. Wang, *Energy Environ. Sci.* **2013**, *6*, 3576; b) S. Niu, Z. L. Wang, *Nano Energy* **2015**, *14*, 161.

[20] a) Y. Bai, H. Feng, Z. Li, *Cell Rep. Phys. Sci.* **2022**, *3*, 101108; b) B. Yang, W. Zeng, Z. H. Peng, S. R. Liu, K. Chen, X. M. Tao, *Adv. Energy Mater.* **2016**, *6*, 1600505; c) X. Zhang, X. Yan, F. Zeng, H. Zhang, P. Li, H. Zhang, N. Li, Q. Guan, Z. You, *Adv. Sci. (Weinh)* **2025**, *12*, 2412258.

[21] Z. Peng, C. Wang, L. Chen, S. Chen, *Int. J. Solids Struct.* **2014**, *51*, 4596.

[22] a) Y. Kim, D. Lee, J. Seong, B. Bak, U. H. Choi, J. Kim, *Nano Energy* **2021**, *84*, 105925; b) C. Zhang, L. Zhou, P. Cheng, X. Yin, D. Liu, X. Li, H. Guo, Z. L. Wang, J. Wang, *Appl. Mater. Today* **2020**, *18*, 100496.

[23] a) V. Nguyen, R. Yang, *Nano Energy* **2013**, *2*, 604; b) Q. Zhou, K. Lee, K. N. Kim, J. G. Park, J. Pan, J. Bae, J. M. Baik, T. Kim, *Nano Energy* **2019**, *57*, 903.

[24] a) S. Noimark, R. J. Colchester, R. K. Poduval, E. Maneas, E. J. Alles, T. Zhao, E. Z. Zhang, M. Ashworth, E. Tsolaki, A. H. Chester, N. Latif, S. Bertazzo, A. L. David, S. Ourselin, P. C. Beard, I. P. Parkin, I. Papakonstantinou, A. E. Desjardins, *Adv. Funct. Mater.* **2018**, *28*, 1704919; b) H. Yoon, J. Choi, J. Kim, J. Kim, J. Min, D. Kim, S. Jeong, J. G. Lee, J. Bang, S. H. Choi, Y. Jeong, C. Y. Kim, S. H. Ko, *Adv. Funct. Mater.* **2024**, *34*, 2313504.

[25] a) C. Pang, J. K. Kim, Y. Wu, M. Y. Wang, H. Yu, M. Sitti, *Adv. Funct. Mater.* **2023**, *33*, 2303116; b) P. Zhang, S. Zhang, X. Li, T. Liu, T. Zhao, J. Wang, B. Luo, C. Cai, Y. Liu, Y. Shao, G. Du, S. Wang, S. Nie, *Adv. Funct. Mater.* **2024**, *35*, 2311993; c) M. Seong, C. Park, J. Kim, M. Kim, J. Song, H. N. Kim, J. G. Ok, H. E. Jeong, *Materials Today Nano* **2024**, *27*, 100488; d) B. Park, C. Jeong, J. Ok, T. I. Kim, *Chem. Rev.* **2024**, *124*, 6148; e) L. Wang, K.-H. Ha, G. J. Rodin, K. M. Liechti, N. Lu, *Frontiers in Mechanical Engineering* **2020**, *6*, 601510.

[26] a) K. Barri, P. Jiao, Q. Zhang, J. Chen, Z. Lin Wang, A. H. Alavi, *Nano Energy* **2021**, *86*, 106074; b) H. Tao, J. Gibert, *Adv. Funct. Mater.* **2020**, *30*, 2001720; c) X. Xu, Q. Wu, Y. Pang, Y. Cao, Y. Fang, G. Huang, C. Cao, *Adv. Funct. Mater.* **2021**, *32*, 2107896; d) M. Yuan, W. Yao, Z. Ding, J. Li, B. Dai, X. Zhang, Y. Xie, *Nano Energy* **2024**, *122*, 109328; e) M. Yuan, W. Yu, Y. Jiang, Z. Ding, Z. Zhang, X. Zhang, Y. Xie, *Nano Energy* **2022**, *103*, 107773.

[27] a) J. Han, J. Li, X. Zhang, L. Zhao, C. Wang, *Chem. Eng. J.* **2024**, *489*, 151493; b) H. Wu, X. Liu, W. Li, S. Kang, B. Zhu, L. Yang, R. Liao, Z. An, J. Wang, *Nano Energy* **2024**, *123*, 109441.

[28] B. Shin, Y. Kwon, M. Mittaz, H. Kim, X. Xu, E. Kim, Y. J. Lee, J. Lee, W. H. Yeo, H. J. Choo, *Nat. Commun.* **2024**, *15*, 6803.

[29] a) W. Cho, S. Kim, H. Lee, N. Han, H. Kim, M. Lee, T. H. Han, J. J. Wie, *Adv. Mater.* **2024**, *36*, 2404163; b) H. Gao, M. Hu, J. Ding, B. Xia, G. Yuan, H. Sun, Q. Xu, S. Zhao, Y. Jiang, H. Wu, M. Yuan, J. Li, B. Li, J. Zhao, D. Rao, Y. Xie, *Adv. Funct. Mater.* **2023**, *33*, 2213410; c) Z. Wang, D. Wu, M. Chi, X. Zou, J. Wang, T. Zhao, H. Zhang, Y. Zhu, K. Jiang, F. Meng, S. Wang, S. Nie, *Adv. Funct. Mater.* **2024**, *35*, 2413719.